Chinese Chemical Letters 37 (2026) 111341

Contents lists available at ScienceDirect

Chinese Chemical Letters

journal homepage: www.elsevier.com/locate/cclet

Pyromellitic diimide induced TiO_2 mesocrystals with oxygen vacancies for synergistic photocatalytic H_2O_2 production and antibiotics degradation

Zhiling Du [a], Zhiqi Zhou [a], Nan Sun [a], Cailiang Yue [a,b], Fuqiang Liu [a,b,*]

[a] School of Environment, Nanjing University, Nanjing 210023, China
[b] Key Laboratory of Agro-Forestry Environmental Processes and Ecological Regulation of Hainan Province, School of Environmental Science and Engineering, Hainan University, Haikou 570228, China

ARTICLE INFO

Article history:
Received 6 February 2025
Revised 14 May 2025
Accepted 16 May 2025
Available online 17 May 2025

Keywords:
Photocatalysis
Oxygen vacancy
Mesocrystal
Hydrogen peroxide
Antibiotics

ABSTRACT

Photocatalytic H_2O_2 production has emerged as a promising strategy for solar-to-H_2O_2 energy conversion. However, the inevitable requirement for aeration or sacrificial agents poses great challenges for its further application, particularly in environmental remediation process. Previous works often struggles to simultaneously balance the antibiotics degradation and H_2O_2 production. Herein, bifunctional TiO_2 mesocrystal with oxygen vacancy (meso–TiO_{2-x}) was prepared through a facile pyromellitic diimide assisted hydrothermal process. The well-aligned meso–TiO_{2-x} superstructures with unique oxygen vacancies on the surface collectively facilitated the direct h^+ oxidation and oxygen reduction reaction (ORR). The ciprofloxacin degradation through direct h^+ oxidation boosted the separation of photogenerated carriers, which enhances the e- participation in ORR, resulting H_2O_2 production rate up to 904.2 μmol g^{-1} h^{-1}. This work provides an ingenious strategy of constructing bifunctional catalyst to achieve synergistic antibiotics degradation and H_2O_2 production without the addition of exogenous reagents.

© 2025 Published by Elsevier B.V. on behalf of Chinese Chemical Society and Institute of Materia Medica, Chinese Academy of Medical Sciences.

H_2O_2 is recognized as a green oxidant and finds extensive applications in industrial processes, chemical synthesis, and environmental application [1]. The predominant method for the commercial production of H_2O_2 is the anthraquinone process. However, this method suffers from harsh reaction conditions and high energy consumption, which limits its widespread application [2]. In recent years, the solar-to-H_2O_2 energy conversion has emerged as a promising alternative for H_2O_2 production. In this approach, photogenerated e^- from light excitation participates in oxygen reduction reaction (ORR) to yield H_2O_2 (Eqs. 1 and 2) [3]. Zhang *et al.* proposed resin-based photo-self-Fenton system in which H_2O_2 was photocatalytic produced and activated into $^{\bullet}OH$ for bisphenol A degradation [4]. Typically, the reaction between h^+ and H_2O (Eq. 2) is thermodynamically and kinetically challenging, leading to insufficient e^--h^+ separation, which subsequently hinders the ORR. Consequently, the requirement for aeration or sacrificial agents addition remains inevitable in previous reported works, which increases operation costs and complexity [5–7]. Actually, the direct oxidation by h^+ earns a crucial place in antibiotics degradation. Conversely, antibiotics could also trigger the h^+ scavenging effect, thereby promoting the ORR without the need for the addition of exogenous reagents. In this regard, we conceive of constructing dual sites for both direct h^+ oxidation and ORR, thereby enabling the synergistic antibiotics degradation and H_2O_2 production.

$$O_2 + 2H^+ + 2e^- \rightarrow H_2O_2 \quad (1)$$

$$2H_2O + 4h^+ \rightarrow O_2 + 4H^+ \quad (2)$$

TiO_2, a widely studied photocatalyst, exhibits excellent redox properties and is considered as a promising candidate for the construction of bifunctional catalytic materials. However, it still suffers from limitations such as low mass transfer efficiency and insufficient O_2 affinity [8]. Crystallization by particle attachment, wherein appropriately selected precursor serve as fundamental building blocks for oriented assembly into mesocrystals, offers a potential solution [9]. Mesocrystals are characterized as superstructures of well-aligned nanoparticles, typically exhibiting regular morphology, uniform size, and excellent porosity [10]. In addition, vacancy engineering has been proved a powerful strategy to improve the photocatalytic performance. For instance, oxygen vacancies (Ov)

* Corresponding author.
E-mail address: lfq@nju.edu.cn (F. Liu).

https://doi.org/10.1016/j.cclet.2025.111341
1001-8417/© 2025 Published by Elsevier B.V. on behalf of Chinese Chemical Society and Institute of Materia Medica, Chinese Academy of Medical Sciences.

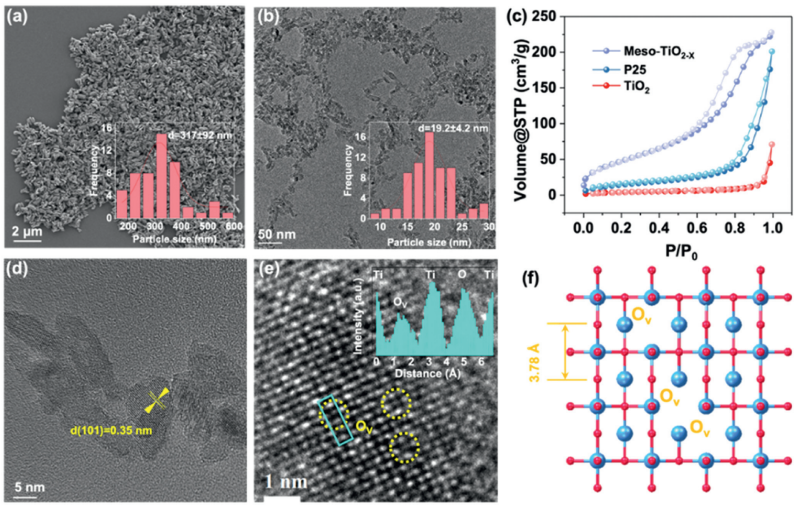


Fig. 1. (a) SEM image of TiO_2 and (b) TEM image of meso–TiO_{2-x}. (c) N_2 adsorption-desorption isotherms. (d, e) HRTEM images and intensity analysis (inset) of meso–TiO_{2-x}. (f) Schematic illustration of Ov in meso–TiO_{2-x}.

can serve as shallow electron acceptors for electron-rich molecules, thereby enhancing O_2 affinity for ORR [11]. Hence, constructing TiO_2 mesocrystals with rich Ov could simultaneously realize antibiotics degradation and H_2O_2 production.

In this work, TiO_2 mesocrystals with Ov (meso–TiO_{2-x}) were successfully prepared through a facile pyromellitic diimide (PDI)-assisted hydrothermal process. Comprehensive characterizations were conducted to elucidate the detailed structure of the catalyst. The photocatalytic H_2O_2 production and ciprofloxacin (CIP, a fluoroquinolone antibiotic, chosen as a model pollutant) degradation were thoroughly investigated. Scavenger experiments and electron paramagnetic resonance (EPR) spectroscopy were employed to determine the primary reactive species involved. Additionally, density functional theory (DFT) calculations were carried out to reveal the underlying mechanisms responsible for the enhanced performance of meso–TiO_{2-x}. Overall, this study developed a bifunctional photocatalyst for synergistic antibiotics degradation and H_2O_2 production. The detailed information for chemicals and materials, catalysts preparation, characterization and analytic methods was presented in Texts S1-S6 (Supporting information). PDI-x represented as catalysts with a mass ratio (Ti-glycerol/PDI) of x. Specially, PDI-0 and PDI-6 were pristine TiO_2 and meso–TiO_{2-x}, respectively.

The microstructures of TiO_2 and meso–TiO_{2-x} were investigated using scanning electron microscopy (SEM) and transmission electron microscopy (TEM) in Figs. 1a and b. The pristine TiO_2 showed larger particle sizes with uneven size distribution. while meso–TiO_{2-x} exhibited a regular morphology with uniform particle size, which could be attributed to the superstructures of well-aligned mesocrystals. The hydrolysis of the imide bonds in the PDI structure generated carboxyl groups, which chelated with Ti, thereby providing nucleation sites for TiO_2 growth. This process effectively prevented the extensive aggregation of crystals, promoting uniform crystal growth, reducing particle size, and leading to the formation of mesocrystals. BET analysis in Fig. 1c, Fig. S1 and Table S1 (Supporting information) indicated that meso–TiO_{2-x} had higher porosity compared to TiO_2, with surface areas of 177.1 and 15.4 m^2/g, respectively. The TEM images (Fig. 1d) revealed a lattice spacing of 0.35 nm, corresponding to the (101) crystal plane of anatase TiO_2 [12]. Furthermore, high-resolution TEM image showed a sharp contrast in intensity analysis, suggesting the existence of O_V, as highlighted in the yellow circle (Fig. 1e). As evidenced in the structural model (Fig. 1f), the center distance of 3.78 Å corresponded to the oxygen atom, indicating the Ov exposed on the surface of anatase TiO_2. Energy dispersive spectroscopy (EDS) mappings in Fig. S2 (Supporting information) confirmed the uniform distribution of N, C, Ti, and O elements on the surface, validating the participation of PDI in the formation of meso–TiO_{2-x}.

The X-ray diffraction (XRD) patterns (Fig. 2a) indicated that the pristine TiO_2, synthesized without PDI (PDI-0), exhibited a brookite crystal structure. As the amount of PDI increased, TiO_2 gradually transitioned from brookite to anatase. Upon the addition of PDI, the pH of the hydrothermal solution decreased from 13 to 8–9. As the hydrothermal reaction progressed, PDI continued to react and hydrolyze, leading to a further pH decrease, ultimately falling below 4 (Fig. 2b). In the hydrothermal process, Ti^{4+} formed complex octahedral configuration with OH^- or O^{2-}. With the pH decrease, OH^- on the surface of growth units was replaced by O^{2-}, which impeded the surface hydroxylation and promoted the growth of long chain polymers to form anatase TiO_2. Consequently, the pH reduction caused by the hydrolysis of the imide bonds in PDI was the main factor driving the crystal phase transition of TiO_2 [13]. In the solid-state EPR spectra (Fig. 2c), the signal at $g = 2.003$ corresponds to e^- trapped by Ov [14]. The stronger EPR signal observed in meso–TiO_{2-x} compared to TiO_2 further confirmed the formation of Ov. The binding energy of the O 1s X-ray photoelectron spectra (XPS) in Fig. 2d exhibited peaks corresponding to lattice O (529.7 eV), -OH (532.2 eV), and adsorbed O_2 (536.2 eV) [15]. The introduction of PDI induced the emergence of new characteristic peaks attributed to Ov adsorbed oxygen species, whose intensity exhibited a positive correlation with the PDI amount. Additionally, the negative shift observed in the Ti 2p spectra (Fig. 2e) suggested an increase in the electronic density of Ti due to the absence of adjacent O atoms [16]. These findings provided compelling evidence for the present of Ov, which was consistent with the HRTEM results. Photoelectric measurements were performed to evaluate the photoelectric properties of the catalysts. As displayed in UV–vis diffuse reflectance (DRS) spectra (Fig. 2f), meso–TiO_{2-x} exhibited enhanced light absorption in the range of 400–800 nm, with two distinct absorption edges, which may be attributed to midgap energy level induced by Ov [17]. According to the Kubelka-Munk formula, the energy band corresponding to these two absorption edges were calculated to be 2.44 and 3.20 eV, respectively. The valence band potential of meso–TiO_{2-x} was 2.07 eV as manifested by XPS-VB spectrum in Fig. S3 (Supporting information). And the conduction band potential was determined as −1.20 eV in Mott-Schottky curves (Fig. S4 in Supporting information) [18]. Steady-

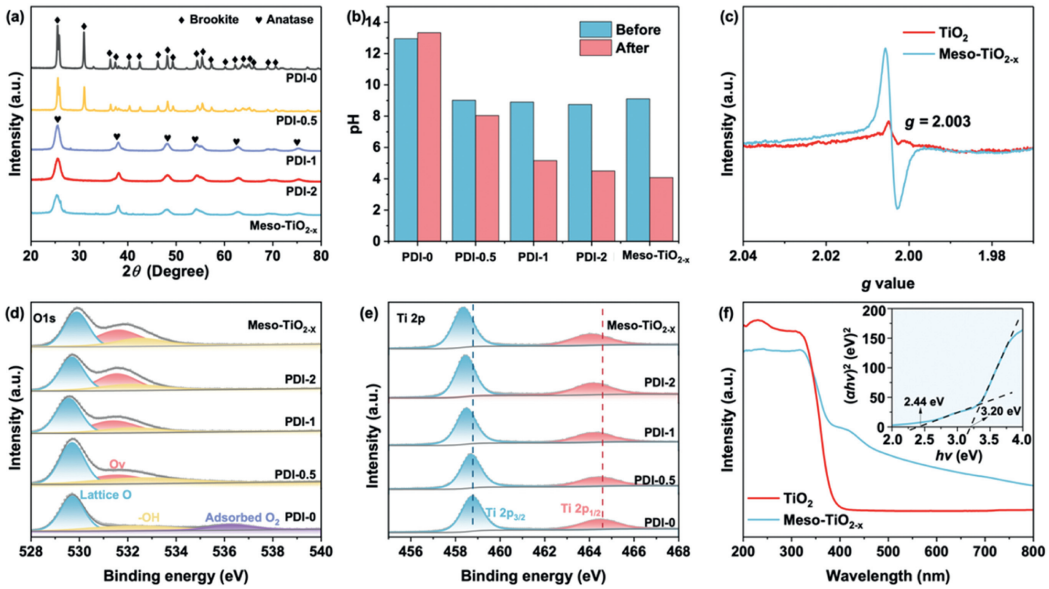


Fig. 2. (a) XRD patterns of catalysts with different PDI amount. (b) pH variation before and after hydrothermal process. (c) Solid EPR spectra of TiO_2 and meso–TiO_{2-x}. XPS spectra for O 1s (c) and Ti 2p (d) of catalysts with different PDI amount. (f) UV–vis DRS spectra of TiO_2 and meso–TiO_{2-x}.

state photoluminescence (PL) spectroscopy, presented in Fig. S5a (Supporting information), revealed a significant decrease in the PL intensity for meso–TiO_{2-x}, suggesting a reduction in the recombination of photogenerated carriers. Time-resolved PL measurements (Fig. S5b and Table S2 in Supporting information) further indicated that the carrier lifetimes for TiO_2 and meso–TiO_{2-x} were 11.94 and 4.7 ns, respectively. The Ov acted as electron traps, thereby reducing the carrier lifetime and mitigating the issue of carrier recombination [19]. As shown Fig. S5c (Supporting information), the smaller arc radius in the Nyquist plots for meso–TiO_{2-x} indicated a lower charge transfer resistance. Additionally, photocurrent measurements (Fig. S5d in Supporting information) under intermittent irradiation further confirmed the higher carrier transfer rate of meso–TiO_{2-x}.

The catalytic performance of the as-synthesized catalysts was initially assessed through the photocatalytic degradation of ciprofloxacin (CIP) (Fig. 3a). UV–vis irradiation alone was ineffective in removing CIP (<11.9 %), indicating that the direct photolysis of CIP was negligible. And meso–TiO_{2-x} alone resulted in only a 35.1 % removal *via* adsorption. In contrast, the combination of the catalysts and UV–vis led to a substantial CIP degradation. The catalytic performance of catalysts with different amount of PDI was evaluated (Fig. 3b), the trend of the *pseudo*-first-order kinetic rate constants (k) first decreased and then increased, with a considerable k value of 0.068 min^{-1} observed for meso–TiO_{2-x}. Besides the contribution of Ov, the increased specific surface area of anatase mesocrystals induced by PDI, which facilitated mass transfer, also accounted for the enhanced performance. Moreover, the photocatalytic degradation of CIP over meso–TiO_{2-x} was tested in various water matrices, including tap water, Yangshan lake, and Qinhuai river (Table S3 in Supporting information). As demonstrated in Fig. 3c, the degradation of CIP was minimally affected, with complete removal occurring within 60 min. The effect of initial pH, catalyst dosage and co-existing substances on CIP degradation were systematically investigated. Complete removal of CIP was achieved within 40 min across a wide pH range of 4–11 (Fig. S6 in Supporting information). Also, effective CIP degradation could be maintained in the presence of coexisting inorganic anions (Cl^-, SO_4^{2-} and NO_3^-) and NOM (natural organic matter) (Fig. S7 in Supporting information). Besides, considering the aggregation and light shading effect, the optimal catalyst dosage was 0.2 g/L (Fig. S8 in Supporting information). The catalytic performance of meso–TiO_{2-x} showed no significant decline in activity across five consecutive cycles (Fig. 3d). It could be seen from the XRD patterns of fresh and used catalyst (Fig. S9 in Supporting information), the structure of meso–TiO_{2-x} maintained good stability. In addition to CIP, the photocatalytic degradation was also efficient for various antibiotics, such as tetracycline (TC), norfloxacin (NOR) and ofloxacin (OFL) (Fig. 3e). However, the adsorption and degradation of sulfamethoxazole (SMZ) were unsatisfactory, which might be attributed to the specific active species associated with the bifunctional sites of the catalyst.

Furthermore, the photocatalytic H_2O_2 production was evaluated. As shown in the Fig. S10 (Supporting information), PDI and TiO_2 could hardly produce H_2O_2 in the absence of aeration and sacrificial agent. The H_2O_2 production of commercial anatase TiO_2 (a-TiO_2) was merely 34.3 μmol g^{-1} h^{-1}. In contrast, the photocatalytic H_2O_2 yield over meso–TiO_{2-x} reached 387.5 μmol g^{-1} h^{-1} under pure water condition, demonstrating that Ov significantly enhanced the production of H_2O_2. Besides, the formation rate constant (k_f) and decomposition rate constant (k_d) were calculated in Fig. 3f and Fig. S10 (Supporting information). Meso-TiO_{2-x} exhibited the highest k_f of 7.0 μmol L^{-1} min^{-1}, which was 8748.9, 68.7 and 7.6 times higher than PDI, TiO_2 and commercial anatase TiO_2 (a-TiO_2), respectively. Further, H_2O_2 production under Ar purging was completely suppressed, indicating that H_2O_2 generation primarily originated from the ORR (Fig. 3g). The concentration of dissolved oxygen (DO) after purging Ar was recorded in Fig. S11 (Supporting information). The DO concentrations remained consistently below 0.1 mg/L under both dark and light irradiation conditions, with no significant difference observed between these states. Notably, H_2O_2 production was undetectable in either condition. These results conclusively excluded the possibility of water oxidation reaction (WOR) contributed in the reaction. Purging with O_2 significantly facilitated the ORR, leading to a H_2O_2 yield of 645.8 μmol g^{-1} h^{-1}. Furthermore, the addition of CIP enhanced the H_2O_2 yield to 904.2 μmol g^{-1} h^{-1}, which was 1.4 times higher than that of pure water condition, likely due to the consumption of h^+ by CIP improving the ORR process. Such promoting effect was also existed in TC, SMZ, OFL and NOR, with H_2O_2 production reached 912.5, 579.1, 612.5 and 533.3 μmol g^{-1} h^{-1}, respectively (Fig. S12 in Supporting information). And, the introduction of the commonly

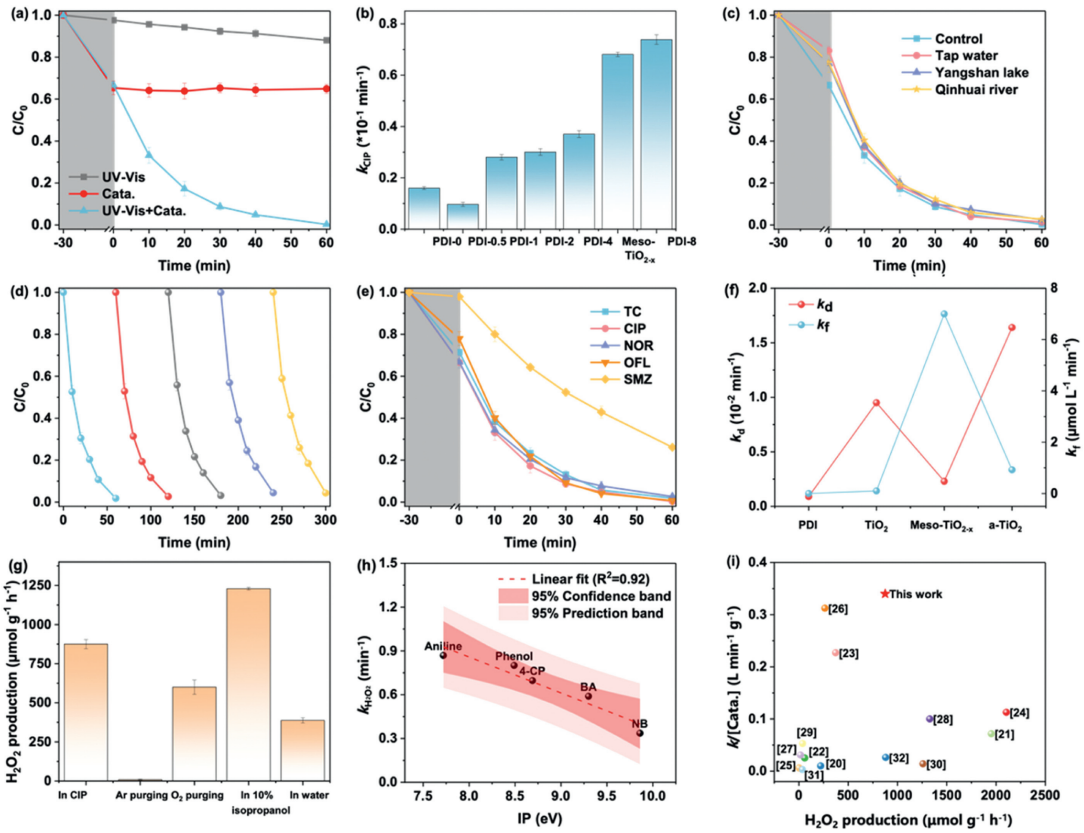


Fig. 3. (a) CIP degradation under different conditions. (b) CIP degradation over catalysts with different PDI amount. (c) CIP degradation over meso–TiO_{2-x} in different water matrices. (d) The cycling performance of meso–TiO_{2-x} for CIP degradation. (e) Various antibiotics degradation over meso–TiO_{2-x}. (f) The k_d and k_f of PDI, TiO_2, meso–TiO_{2-x} and a-TiO_2. (g) Photocatalytic H_2O_2 production under different conditions. (h) The plots of k_{H2O2} with IP. (i) Comparisons of catalytic efficiency of meso–TiO_{2-x} with those of reported works. Reaction conditions: 500 W Xe lamp, [Catalyst] = 0.2 g/L, [Pollutants] = 20 mg/L, pH unadjusted, T = 25 °C (If applied).

used sacrificial agent isopropanol led to a more pronounced increase in H_2O_2 yield due to its higher efficiency in quenching h^+. To validate the conjecture of synergistic interaction between antibiotics degradation and H_2O_2 generation. H_2O_2 production was measured in a series of organics with different ionization potentials (Fig. S13 and Table S4 in Supporting information). It could be seen that the kinetic constant for H_2O_2 production ($k_{H_2O_2}$) was inversely proportional to the ionization potential (IP) of organics (Fig. 3h). Specifically, the lower the ionization potential, the easier it was to lose e^- and be oxidized by h^+, which was more conducive to ORR. This observation further supported that antibiotics degradation and H_2O_2 production were mutually reinforcing processes, exhibiting a synergistic relationship. Comparative analysis was conducted with previous reported works under comparable conditions (Fig. 3i and Table S5 in Supporting information). Notably, previous works often struggled to simultaneously balance the antibiotics degradation and H_2O_2 production. In this study, the construction of bifunctional meso–TiO_{2-x} effectively facilitated the synergistic occurrence of both antibiotics degradation and H_2O_2 production, demonstrating distinct advantages [20–32].

Scavenger experiment was conducted to identify the main active species involved in the CIP degradation. As shown in Fig. 4a, *p*-benzoquinonep (PBQ), *tert*–butyl alcohol (TBA), and furfuryl alcohol (FFA), which act as quenchers for $^{\bullet}O_2^-$, $^{\bullet}OH$ and $^1O_2$, respectively, exhibited minimal inhibition on CIP degradation. In contrast, EDTA-2Na served as a h^+ scavenger, exhibiting significant inhibition, which indicated that CIP degradation primarily relied on the direct oxidation by h^-. Additionally, the introduction of $KBrO_3$ enhanced CIP degradation, as it acted as an e^- scavenger, promoting further separation and oxidation reaction of h^+. Furthermore, the EPR spectra (Fig. 4b) revealed a gradual decrease in the TEMPO signal intensity over time, which could be attributed to the reduction of photogenerated e^-. This observation suggested that the e^--h^+ pairs in the system were effectively separated and actively participated in subsequent redox reactions [33]. Concurrently, the prominent DMPO-$^{\bullet}O_2^-$ signal indicated that $^{\bullet}O_2^-$ was an intermediate product of the ORR (Fig. 4c).

DFT calculations were executed to gain further insight into the underlying mechanism for the function of Ov. The partial and summed density of states (PDOS) was analyzed in Fig. 4d. Compared to pristine TiO_2, a sub-band resulted from Ov state was found in meso–TiO_{2-x}, which in accordance with the DRS results [34]. Moreover, O_2 adsorption mode were evaluated in Fig. 4e. O_2 adsorption was thermodynamically unfavorable on pristine TiO_2 with a positive adsorption energy of 3.48 eV. However, upon the introduction of Ov, the adsorption energy was calculated as −3.66 eV, suggesting that photocatalytic H_2O_2 production *via* the ORR was more favorable on the Ov of meso–TiO_{2-x}. Based on the discussion above, the synergistic CIP degradation and H_2O_2 production was elucidated in Fig. 4f. Upon light stimulation, e^- was excited to the conduction band, leaving h^+ in the valence band, while part of e^- transferred to intermediate levels, which inhibited e^--h^+ recombination. Simultaneously, O_2 adsorbed in Ov to produce H_2O_2 *via* the ORR, while CIP was degraded through the direct oxidation of h^+. This synergistic process of antibiotics degradation and H_2O_2 production was facilitated by the bifunctional properties of meso–TiO_{2-x}.

Liquid chromatography-mass spectrometry (LC-MS) was employed to identify the intermediates formed during CIP degradation, as summarized in Table S6 and Figs. S14-S20 (Supporting information). Accordingly, possible degradation pathways were proposed, as illustrated in Fig. 5a. Initially, CIP degradation pro-

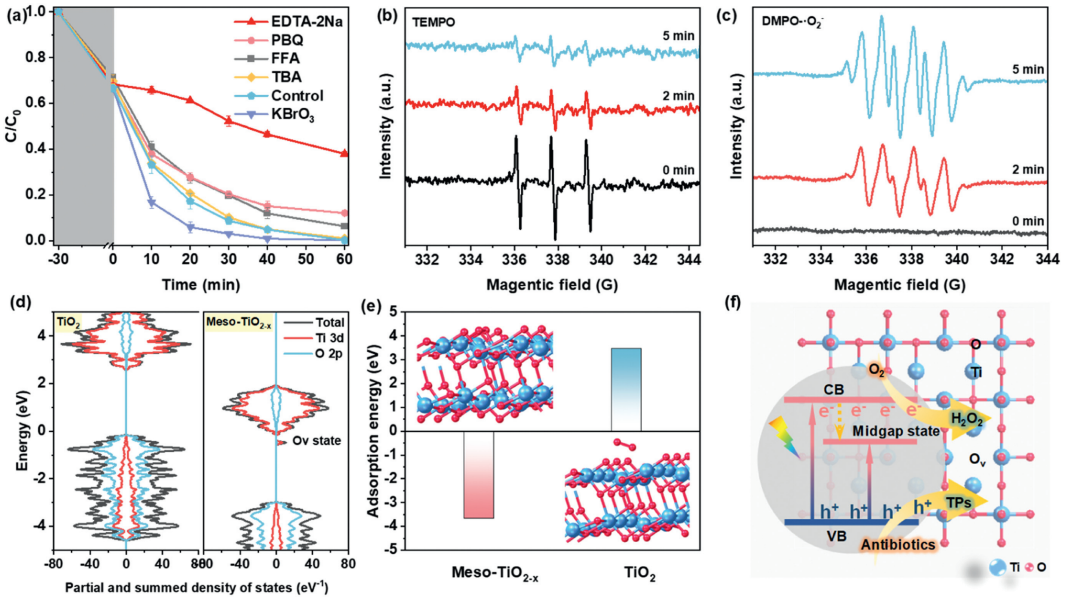


Fig. 4. (a) Effects of scavengers on CIP degradation. EPR spectra for (b) TEMPO and (c) DMPO–O_2^-. (d) PDOS of TiO_2 and meso–TiO_{2-x}. (e) Adsorption energy of O_2 molecule on meso–TiO_{2-x}. (f) Schematic illustration of synergistic antibiotics degradation and H_2O_2 production. Reaction conditions: 500 W Xe lamp, [Catalyst] = 0.2 g/L, [CIP] = 20 mg/L, pH unadjusted, T = 25 °C, [EDTA-2Na] = 10 mmol/L, [PBQ] = 20 mmol/L, [FFA] = 20 mmol/L, [TBA] = 100 mmol/L, [$KBrO_3$] = 10 mmol/L (If applied).

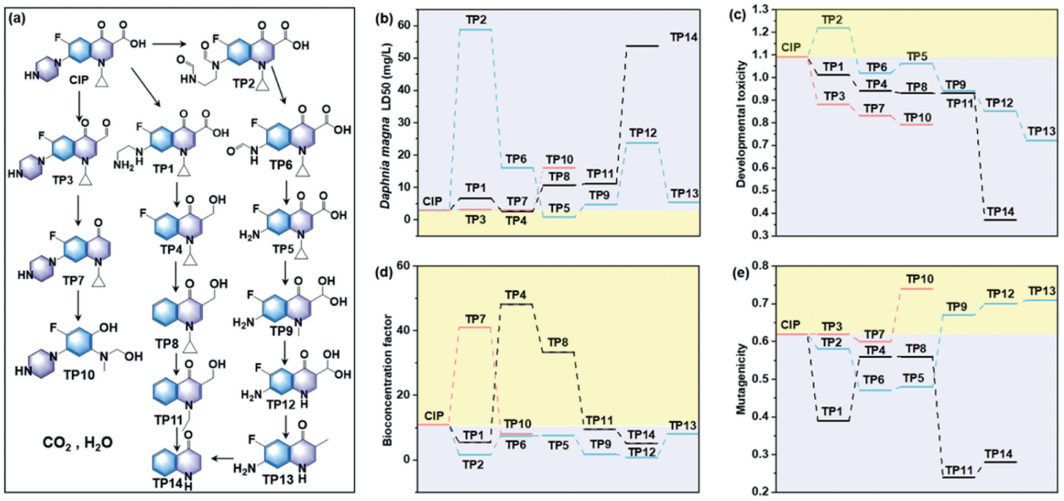


Fig. 5. (a) Intermediate products and possible degradation pathway of CIP. (b) Acute toxicity indexes, (c) developmental toxicity indexes, (d) bioconcentration factor (Value of TP3 was not obtained) and (e) mutagenicity of CIP and degradation intermediates.

ceeded *via* a dihydroxylation reaction, yielding **TP3**. The cleavage of the carbonyl group then produced **TP7**, which subsequently underwent ring-opening to form **TP10**. Additionally, the piperazine group in CIP was cleaved, resulting in the formation of **TP1** and **TP2**. **TP2** further transformed into **TP5**, **TP6** and **TP9**, which were followed by dealkylation and decarboxylation to generate **TP12** and **TP13**. Meanwhile, **TP1** was cleaved into **TP4** and **TP8**. The dissociation of the cyclopropyl group, coupled with decarboxylation, led to the formation of **TP11** and **TP14**. To evaluate the ecotoxicity of the degradation products, key toxicity indicators were assessed using the Toxicity Estimation Software Tool [35]. As shown in Figs. 5b–e, acute toxicity, developmental toxicity, bioconcentration factor, and mutagenicity were significantly alleviated, suggesting that the effluent after treatment was more compatible with environmental release, thus lowering the potential ecological risk.

In conclusion, TiO_2 mesocrystal with Ov was prepared through a facile PDI assisted hydrothermal process. The hydrolysis of the imide bonds in the PDI provided nucleation sites for TiO_2 growth, thus facilitating the formation of mesocrystals. The well-aligned superstructures of meso–TiO_{2-x} renders it excellent porosity for the mass transfer. Besides, the resulted Ov not only served as e^- trap to tackle the carrier recombination issue but also facilitated the O_2 adsorption for ORR. Based on it, photocatalytic H_2O_2 production reached 904.2 μmol g^{-1} h^{-1} without aeration or sacrificial agents. Meanwhile, photocatalytic CIP degradation through h^+ oxidation achieved a k value of 0.068 min^{-1}. Environmental toxicity analysis suggested that ecological risk of CIP was significantly reduced after treatment. Overall, this work proposed a facile strategy of constructing bifunctional photocatalyst for synergistic antibiotics degradation and H_2O_2 production.

Declaration of competing interests

The authors declare that they have no known competing financial interests or personal relationships that could have appeared to influence the work reported in this paper.

CRediT authorship contribution statement

Zhiling Du: Writing – review & editing, Writing – original draft, Validation, Methodology, Investigation, Data curation, Conceptualization. **Zhiqi Zhou:** Validation, Investigation, Data curation. **Nan Sun:** Investigation, Data curation. **Cailiang Yue:** Writing – review & editing, Validation, Software, Methodology, Conceptualization. **Fuqiang Liu:** Writing – review & editing, Supervision, Resources, Project administration, Conceptualization.

Acknowledgment

This work was supported by the National Outstanding Youth Science Fund Project of National Natural Science Foundation of China (No. 51522805).

Supplementary materials

Supplementary material associated with this article can be found, in the online version, at doi:10.1016/j.cclet.2025.111341.

References

[1] Y.F. Bu, R. Ma, Y.B. Wang, Y.X. Zhao, F. Li, et al., Adv. Mater. 36 (2024) 2412670.
[2] H.L. Hou, X.K. Zeng, X.W. Zhang, Angew Chem. Int. Ed. 59 (2020) 17356–17376.
[3] H. Zhang, X.F. Bai, Appl. Catal. B 298 (2021) 120516.
[4] X.D. Zhang, J. Wang, B.B. Xiao, Y.J. Pu, Y.C. Yang, et al., Appl. Catal. B 315 (2022) 121525.
[5] M.Y. Jing, H. Zhao, L. Jian, C.S. Pan, Y.M. Dong, et al., J. Hazard. Mater. 449 (2023) 131017.
[6] J.J. Jiang, S.D. Liu, D.L. Shi, T.Z. Sun, Y.K. Wang, et al., Water Res. 244 (2023) 120502.
[7] J.H. Lee, H. Cho, S.O. Park, J.M. Hwang, Y. Hong, et al., Appl. Catal. B 284 (2021) 119690.
[8] Z.L. Du, C.Q. Zhu, S.C. Jing, C.L. Yue, F.Q. Liu, et al., Chem. Eng. J. 462 (2023) 142146.
[9] Z.S. Hong, M.D. Wei, T.B. Lan, L.L. Jiang, G.Z. Cao, Energ. Environ. Sci. 5 (2012) 5408–5413.
[10] G.M. Zhu, M.L. Sushko, J.S. Loring, B.A. Legg, M. Song, et al., Nature 590 (2021) 211–416.
[11] Y.C. Wang, L.F. Liu, Y.X. Wei, X.S. Xu, G.F. Zhao, et al., ACS Appl. Mater. Inter. 16 (2024) 50879–50886.
[12] C.L. Yue, N. Sun, Y.X. Qiu, L.L. Zhu, Z.L. Du, et al., Chin. Chem. Lett. 35 (2024) 109698.
[13] X.Y. Tong, W. Chen, G. Cheng, Mol. Catal. 560 (2024) 114140.
[14] Y.X. Wang, Y.Y. Zhang, X.J. Zhu, Y. Liu, Z.B. Wu, Appl. Catal. B 316 (2022) 121610.
[15] W. Zhang, H.L. He, Y. Tian, H.Z. Li, K. Lan, et al., Nano. Energy 66 (2019) 104113.
[16] X. Bi, G.H. Du, A. Kalam, D.F. Sun, Y. Yu, et al., Chem. Eng. Sci. 234 (2021) 116440.
[17] J. Wu, X.D. Li, W. Shi, P.Q. Ling, Y.F. Sun, et al., Angew Chem. Int. Ed. 57 (2018) 8719–8723.
[18] J. Xu, Q.Z. Gao, Z.P. Wang, Y. Zhu, Appl. Catal. B 291 (2021) 120059.
[19] Y. He, S. Dai, J.P. Sheng, et al., Proc. Natl. Acad. Sci. U. S. A. 121 (2024) e2322107121.
[20] M.Z. Jin, J. Li, D. Song, F.F. Jing, W.W. Lu, et al., Chemistryselect 9 (2024) 202402724.
[21] M.J. Deng, L.Y. Wang, Z.L. Wen, J. Chakraborty, J.M. Sun, et al., Green Chem. 26 (2024) 3239–3248.
[22] H. Wang, P. Xu, E. Almatrafi, Z.W. Wang, C.Y. Zhou, et al., Environ. Res. 246 (2024) 118200.
[23] W.J. Wang, J.Z. Song, W. J.Ren, J. Wu, Q. Chang, et al., Chem. Eng. J. 490 (2024) 151796.
[24] H.J. Zhu, Y.K. Yang, M.H. Li, L.N. Zou, H.T. Zhao, Rare Metals. 43 (2024) 2695–2707.
[25] J.Y. Wang, J.J. Wang, S.J. Zuo, J.C. Pei, W.P. Liu, et al., Chin. Chem. Lett. 34 (2023) 108157.
[26] G.F. Jiang, X.H. You, B.Y. An, B.J. Zhu, F. Liu, et al., Appl. Surf. Sci. 618 (2023) 156656.
[27] Y.J. Lee, Y.J. Jeong, I.S. Cho, S.J. Park, C.G. Lee, et al., J. Hazard. Mater. 449 (2023) 131046.
[28] T.T. Buu, C.Q. Cong, V.M. Quan, B.K. Ngoc, L.P. Thao, et al., Surf. Interfaces 43 (2023) 103516.
[29] T. Li, X.H. Zhang, C. Hu, X.Y. Li, P. Zhang, et al., J. Environ. Chem. Eng. 10 (2022) 107116.
[30] U. Kumar, J. Kuntail, A. Kumar, R. Prakash, M.R. Pai, et al., Appl. Surf. Sci. 589 (2022) 153013.
[31] L. Tan, Y.M. Chen, D.D. Li, S.B. Wang, Z.M. Ao, Nanomaterials 12 (2022) 12183089.
[32] H. Wang, E. Almatrafi, Z.W. Wang, Y. Yang, T. Xiong, et al., J. Colloid. Interf. Sci. 608 (2022) 1051–1063.
[33] Y. Yang, H.C. Yu, M.Q. Wu, T.T. Zhao, Y.A. Guan, et al., Appl. Catal. B 325 (2023) 122307.
[34] L. Tan, S.M. Xu, Z.L. Wang, Y.Q. Xu, X. Wang, et al., Angew Chem. Int. Ed. 58 (2019) 11860–11867.
[35] H.L. Yang, R.L. Qiu, Y.T. Tang, S.J. Ye, S.H. Wu, et al., Water Res. 231 (2023) 119659.